

On Position Angle Errors in the Tremaine-Weinberg Method

Victor P. Debattista[★]

Astronomisches Institut, Universität Basel, Venusstrasse 7, CH-4102 Binningen, Switzerland

Current address: Institut für Astronomie, ETH Hönggerberg, HPF G4.2, CH-8093, Zürich, Switzerland

Draft version on 2 February 2008

ABSTRACT

I show that Tremaine-Weinberg (TW) measurements of bar pattern speeds are sensitive to errors in the position angle of the disc, PA_{disc} . I use an N -body experiment to measure these errors; for typical random PA_{disc} errors, the resulting scatter in the measured values of the dimensionless bar speed parameter \mathcal{R} (defined as the ratio of the corotation radius to the bar semi-major axis) is of order the observational.

I also consider how the systematic PA_{disc} errors produced by disc ellipticities affect TW measurements. The scatter produced by these errors may be significant, depending on the ellipticity distribution. Conversely, by using the sample of TW observations, I find that an upper limit of the typical disc (density) ellipticity is 0.07 at the 90 per cent confidence level, which is in good agreement with previous measurements.

Taken together, the random and systematic scatter suggest that the intrinsic distribution of \mathcal{R} of gas-poor early-type barred galaxies may be as narrow as that of the gas-rich later-types.

Key words: galaxies: elliptical and lenticular, cD — galaxies: kinematics and dynamics — galaxies: structure — methods: observational

1 INTRODUCTION

Barred (SB) galaxies account for more than half of all high surface brightness disc galaxies (Knapen 1999; Eskridge et al. 2000). Recent observational and theoretical studies have focused on the pattern speed of bars, Ω_p . The quantity of greatest interest is $\mathcal{R} \equiv D_L/a_B$, where D_L is the corotation radius and a_B is the semi-major axis of the bar. A self-consistent bar must have $\mathcal{R} \geq 1$ (Contopoulos 1980); bars with $1.0 \leq \mathcal{R} \leq 1.4$ are termed fast, while slow bars have larger \mathcal{R} . Because bars have strong quadrupole moments, they lose angular momentum efficiently in the presence of a dense dark matter halo (Weinberg 1985), slowing down in the process; fast bars therefore have been interpreted as evidence for maximum discs (Debattista & Sellwood 1998, 2000, but see also Valenzuela & Klypin 2002). Thus the accurate measurement of \mathcal{R} in SB galaxies is of interest.

Bar pattern speeds can be most reliably measured when kinematic data are available. One method relies on the dependence of the gas flow pattern on Ω_p , particularly at the shocks in the bar region. Hydrodynamical simulations can therefore recover Ω_p ; these find fast bars (e.g. van Albada & Sanders 1982; Athanassoula 1992; Lindblad & Kristen

1996; Lindblad et al. 1996; Weiner et al. 2001). An alternative method, which measures Ω_p directly, was developed by Tremaine & Weinberg (1984). Until now, the Tremaine-Weinberg (hereafter TW) method has been applied to a small, but growing, number of SB galaxies (published measurements are listed in Table 1); all cases are consistent with fast bars.

Using 2-D absorption-line spectroscopy of the SB0 galaxy NGC 7079, Debattista & Williams (2003, in progress) show that the value of Ω_p obtained with the TW method is sensitive to small errors in the position angle of the disc, PA_{disc} . This raises the possibility that small errors in PA_{disc} introduce a significant scatter in TW measurements of \mathcal{R} .

Errors in PA_{disc} can be either simple random ones, or systematic ones, produced, for example, by deprojecting an intrinsically elliptical disc assuming it is axisymmetric. Constraints on the ellipticities[†] of discs come from a variety of measurements. The observed axes-ratios of galaxies show

[†] In this paper, disc ellipticity refers to the ellipticity, ϵ_D , of the disc's density in its main plane. Expressions relating ϵ_D and ϵ_Φ , the ellipticity of the potential in the disc plane, can be found in Franx et al. (1994). Where the disc dominates the potential, $\epsilon_D > \epsilon_\Phi$.

[★] email: debattis@phys.ethz.ch

a deficit of apparently circular discs, from which one concludes that perfect oblate spheroids are poor fits to the data (Binney & de Vaucouleurs 1981; Groshol 1985). Nevertheless, such studies find that typical ellipticities must be small, $\epsilon_D \lesssim 0.1$ (Magrelli et al. 1992; Huizinga & van Albada 1992; Lambas et al. 1992; Fasano et al. 1993). Constraints on ϵ_D are improved when kinematic data are included. Rix & Zaritsky (1995) defined a sample of 18 kinematically face-on galaxies from the Tully-Fisher relation (Tully & Fisher 1977, hereafter the TF relation). Using K' -band photometry, they estimated typical $\epsilon_\Phi = 0.05^{+0.03}_{-0.02}$, with two arm spirals possibly accounting for some of this signal. Franx & de Zeeuw (1992) showed that the small scatter in the TF relation requires that $\epsilon_\Phi \leq 0.1$. Since it is highly unlikely that all the TF scatter is due to disc ellipticities alone, they concluded that a more likely limit is $0 \leq \epsilon_\Phi \leq 0.06$. By analysing the residuals in the velocity-field of the gas ring around the S0 galaxy IC 2006, Franx et al. (1994) found $\epsilon_\Phi = 0.012 \pm 0.026$ for this galaxy. This approach has also been used by Schoenmakers et al. (1997) ($\epsilon_\Phi < 0.1$ for 2 galaxies) and Beauvais & Bothun (1999), ($\epsilon_D \lesssim 0.08$ for 6 galaxies). An important uncertainty in this method is the viewing angle of any ellipticity. Andersen et al. (2001), therefore, measured ϵ_D from the discrepancies between photometric and kinematic disc parameters of nearly face-on galaxies, finding an average $\epsilon_D = 0.05$ for 7 galaxies; using the same method on a larger sample of 28 galaxies, Andersen & Bershadsky (2002) were able to fit a log-normal distribution, with $\ln \epsilon_D \pm \sigma_{\ln \epsilon} = -2.82 \pm 0.73$ ($\overline{\epsilon_D} = 0.06^{+0.06}_{-0.03}$). In all these studies, spirals may be responsible for some or all of the signal seen (Barnes & Sellwood 2003). Finally, in the Milky Way Galaxy, a variety of constraints, local and global, independently suggest $\epsilon_\Phi \simeq 0.1$, with the Sun close to the minor-axis of the potential (Kuijken & Tremaine 1994).

This paper studies the effect of PA_{disc} errors on TW measurements. In Section 2 I describe the TW method and its main sources of uncertainty. Most of these uncertainties can be quantified directly from observations. However, this is not generally true for errors due to PA_{disc} uncertainties, so that some modelling is required. Section 3 therefore is devoted to setting up an N -body model for studying the impact of PA_{disc} errors on TW measurements. In Section 4 I demonstrate the sensitivity of the TW method to small PA_{disc} errors and estimate the scatter in \mathcal{R} expected for the observational level of PA_{disc} uncertainty. In Section 5, I consider the scatter in \mathcal{R} due to non-axisymmetric outer discs on TW measurements. I also obtain a novel constraint on ϵ_D of early-type SB galaxies, based on the requirement that none of the TW measurements thus far would have found a value of \mathcal{R} outside some range. The result is in agreement with previous determinations of ϵ_D for unbarred galaxies. In Section 6, I present my conclusions. Throughout, I pay particular attention to obtaining a conservative estimate of the scatter in \mathcal{R} due to PA_{disc} errors.

2 THE TW METHOD AND ITS SOURCES OF ERRORS

The TW method requires a tracer population which satisfies the continuity equation, and assumes that the time-

Table 1. The sample of TW measurements in SB galaxies. The references are: Kent 1987 (K87), Merrifield & Kuijken 1995 (MK95), Gerksen et al. 1999 (GKM99), Debattista et al. 2002a (DCA02) and Aguerri et al. 2003 (ADC03). The 6 galaxies from Debattista et al. (2002a) and Aguerri et al. (2003), which have been analysed uniformly, constitute the ADC sample.

Galaxy	i	ψ_{bar}	\mathcal{R}	References
NGC 936	41°	66°	1.4 ± 0.3	K87; MK95
NGC 4596	38°	56°	$1.2^{+0.4}_{-0.2}$	GKM99
NGC 1023	66°	78°	$0.8^{+0.4}_{-0.2}$	DCA02
ESO 139-G009	46°	77°	$0.8^{+0.3}_{-0.2}$	ADC03
IC 874	39°	70°	$1.4^{+0.7}_{-0.4}$	ADC03
NGC 1308	36°	60°	$0.8^{+0.4}_{-0.2}$	ADC03
NGC 1440	38°	40°	$1.6^{+0.5}_{-0.3}$	ADC03
NGC 3412	55°	84°	$1.5^{+0.6}_{-0.3}$	ADC03

dependence of the surface density, Σ , can be expressed, in terms of cylindrical coordinates (R, ϕ) in the disc plane, as:

$$\Sigma = \Sigma(R, \phi - \Omega_p t). \quad (1)$$

While not all non-axisymmetric structures obviously satisfy the condition of equation 1 (*e.g.* warps), bars are well approximated by this assumption. The TW method is then contained in the following expression:

$$\mathcal{X}\Omega_p = \mathcal{V}/\sin i. \quad (2)$$

Here, $\mathcal{X} = \int h(Y) X \Sigma dX dY$, $\mathcal{V} = \int h(Y) V_{\text{los}} \Sigma dX dY$, i is the disc inclination (I use the convention $i = 0$ for face-on), $h(Y)$ is an arbitrary weighting function, V_{los} is the line-of-sight velocity (minus the systemic velocity) and (X, Y) are galaxy-centered coordinates measured along the disc's major (*i.e.* inclination/line-of-nodes) and minor axes, respectively. Equation 2 holds even when $\Omega_p = \Omega_p(t)$, as it must, since the continuity equation is purely kinematic.

Hydrodynamical studies find a narrow range in $\mathcal{R} = 1.2 \pm 0.2$. The quoted errors and spread in \mathcal{R} when measured with the TW method are larger (see Table 1). Important sources of uncertainty in TW measurements are:

(i) *Uncertainty in Ω_p .* To obtain Ω_p with the TW method, the most commonly used strategy is to obtain several absorption-line slit spectra, for each of which \mathcal{V} and \mathcal{X} are measured. Then plotting \mathcal{V} versus \mathcal{X} , one obtains $\Omega_p \sin i$ as the slope of the best-fitting straight line. The values of \mathcal{X} are usually quite well defined; however values of \mathcal{V} tend to be noisy, and are the main source of uncertainty in Ω_p . This problem can be partly alleviated by projecting slit spectra along the spatial direction, thereby increasing the signal-to-noise (S/N) ratio (Merrifield & Kuijken 1995).

(ii) *Uncertainty in V_c .* Once Ω_p is measured, D_L can be approximated as V_c/Ω_p , where V_c may be assumed flat. However, because the tracer population must satisfy the continuity equation, the TW method is applied to early-type galaxies, which lack substantial patchy obscuring dust. Unfortunately, their velocity dispersions are large, so that measurements of V_c require correction for the asymmetric drift (unless gas is present outside the bar region [Gerksen 2002]).

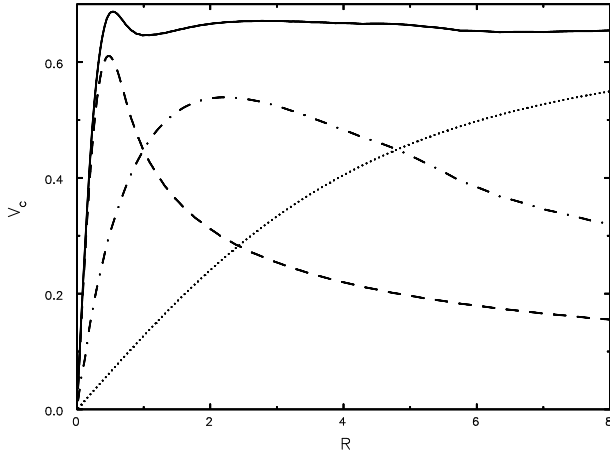


Figure 1. The initial rotation curve of the N -body model used. The dashed, dot-dashed, and dotted lines represent the bulge, disc and frozen halo components respectively, while the solid line is the full rotation curve.

(iii) *Uncertainty in a_B .* The bar semi-major axis is sometimes hard to measure in early-type galaxies since their bars often gradually blend into the disc. The presence of massive bulges further complicates measurement of a_B .

For concreteness, note that the mean fractional uncertainties in Ω_p , V_c and a_B for the ADC sample (defined in Table 1) are 30, 7 and 19 per cent, respectively. The resulting 67 per cent uncertainty in \mathcal{R} , averaged over all the galaxies of Table 1, is $\Delta_{\mathcal{R},unc} = 0.7$. (Meanwhile, the scatter of \mathcal{R} for the full sample, which includes both an observational error part and an intrinsic distribution part, is $\Delta_{\mathcal{R},obs} = 1.0$. I measured this value by using Monte-Carlo experiments in which I varied V_c and a_B uniformly in their error intervals, and varied Ω_p assuming its errors are Gaussian.)

Another source of error in the TW method is errors in the position angle of the disc, PA_{disc} . Consider a slit observation: the right-hand side of equation 2 then measures the flux of the tracer across the slit. However, this requires that the slit be exactly parallel to the X axis; for any other orientation, the observed velocities do not measure the full flux. At the same time, \mathcal{X} , the luminosity-weighted average position along the slit, is rotated by the PA_{disc} error. The combination of these two effects leads to an error in the measured Ω_p . Indeed, it is surprising just how sensitive the TW method is to errors in PA_{disc} : using 2-D Fabry-Perot observations of NGC 7079, Debattista & Williams (2003, in preparation) show that errors of as little as 5° in PA_{disc} can lead to errors in Ω_p of up to 100 per cent. Published values of PA_{disc} often have uncertainties of this order. While uncertainties in Ω_p , a_B and V_c can be quantified directly from observations, errors in \mathcal{R} due to PA_{disc} errors can only be modelled.

3 MODEL AND TW MEASUREMENTS

3.1 The N -body system

To quantify better the sensitivity of the TW method to errors in PA_{disc} , I applied it to a high resolution N -body bar. In numerical simulations, Ω_p can be measured accurately

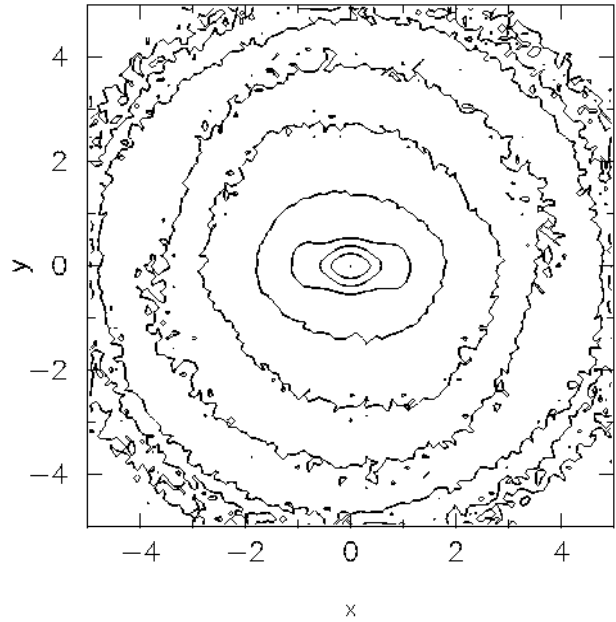


Figure 2. Logarithmically spaced contours of the disc + bulge surface density at $t = 200$. The system is rotating in the counter-clockwise sense.

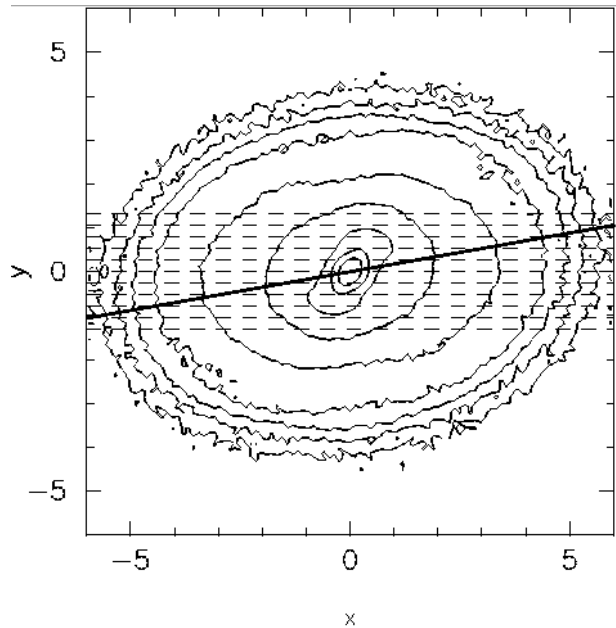


Figure 3. The system after rotation through $\psi_{\text{bar}} = 60^\circ$, $i = 45^\circ$ and $\delta\text{PA} = +10^\circ$. The solid line indicates the disc's true major axis, while the dashed lines indicate the (misaligned) slits used.

directly from the time evolution, which makes possible a comparison with TW measurements at various disc and bar orientations and errors in PA_{disc} . The simulation which produced the model of an early-type galaxy consisted of live disc and bulge components inside a frozen halo. The frozen halo was represented by a spherical logarithmic potential

$$\Phi_L(r) = \frac{1}{2}v_0^2 \ln(r_c^2 + r^2), \quad (3)$$

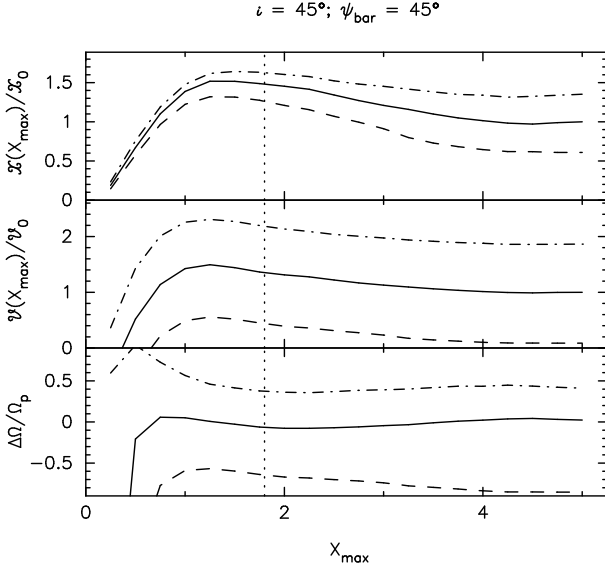


Figure 4. Variation of $\mathcal{X}(X_{\max})$ (top) and $\mathcal{V}(X_{\max})$ (center) with X_{\max} . Each line is normalized by the value of the full integral at $\delta_{\text{PA}} = 0$. The bottom panel shows the resulting fractional errors in the TW measurement of Ω_p using just this one slit. In all panels, the solid, dashed and dot-dashed lines are for $\delta_{\text{PA}} = 0$, $\delta_{\text{PA}} = -5^\circ$ and $\delta_{\text{PA}} = +5^\circ$, respectively. The dotted vertical lines indicate a_B . Other values of ψ_{bar} and i give qualitatively similar results.

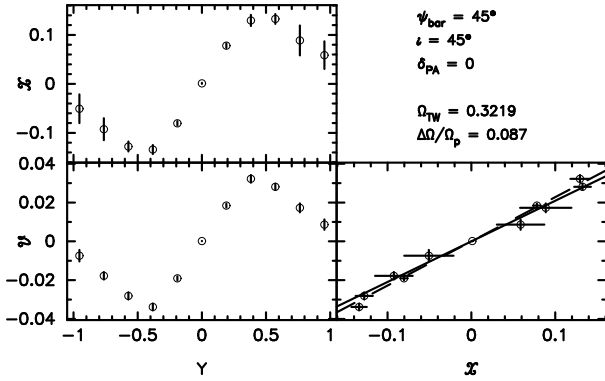


Figure 5. The TW integrals for $\psi_{\text{bar}} = 45^\circ$, $i = 45^\circ$. On the left are shown \mathcal{X} (top) and \mathcal{V} (bottom) as functions of the slit offset. On the right, \mathcal{V} is plotted against \mathcal{X} , and a straight line fit. The solid line has slope $\Omega_p \sin i$ as measured from the time evolution, while the dashed line shows the best-fitting straight line, with slope $\Omega_{\text{TW}} \sin i$. Each slit contains $\gtrsim 10^5$ particles; all errors have been enlarged by a factor of 1000 for clarity.

where r_c is the core-radius and v_0 is the asymptotic circular velocity. The initially axisymmetric disc was modelled by an exponential disc with a Gaussian thickening

$$\rho_d(R, z) = \begin{cases} f_d \frac{M}{2\pi R_d^2} e^{-R/R_d} \frac{1}{\sqrt{2\pi} z_d} e^{-\frac{1}{2}(z/z_d)^2} & R \leq R_t, \\ 0 & R > R_t, \end{cases} \quad (4)$$

where f_d is the fraction of the active mass which is in the disc and R_t is the radius at which the disc is truncated. The bulge was generated using the method of Prendergast & Tomer (1970), where a distribution function is integrated

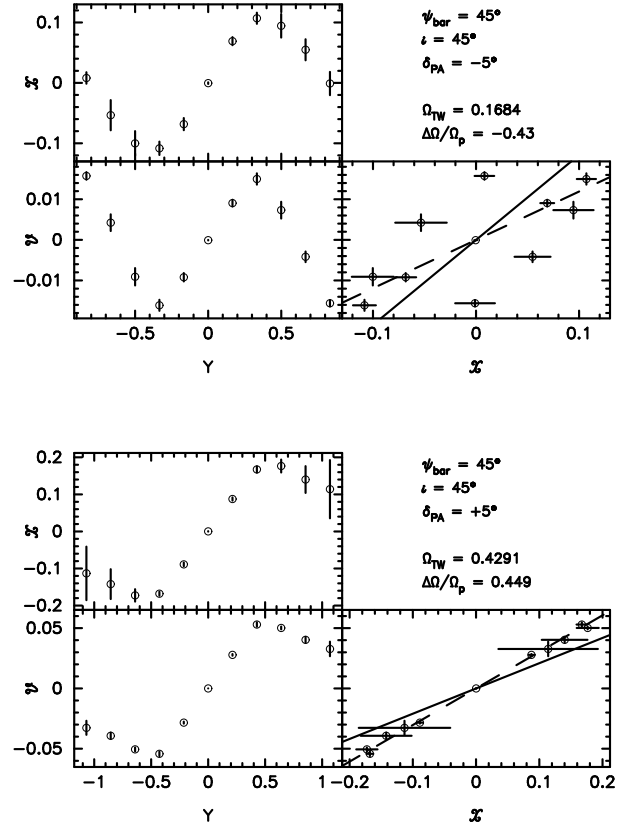


Figure 6. As in Fig. 5 but for $\delta_{\text{PA}} = -5^\circ$ (top 3 panels) and $\delta_{\text{PA}} = +5^\circ$ (bottom 3 panels).

iteratively in the global potential, until convergence. For this application, I used the distribution function of a lowered, $n = 2$, polytrope, truncated at r_b

$$f(x, v) = C \mathcal{F}(E) = C \left\{ [-2E(x, v)]^{1/2} - [-2E_{\max}]^{1/2} \right\}. \quad (5)$$

Here C is a mass normalization constant and $E_{\max} = \Phi_{\text{tot}}(r_b)$, the total potential at r_b in the disc plane. Disc kinematics were set up using the epicyclic approximation to give Toomre $Q = 2.5$, a value appropriate for an early-type disc galaxy; this leads to weak spirals, which do not interfere substantially with measurements of Ω_p . Vertical equilibrium was obtained by integrating the vertical Jeans equation. The disc and bulge were represented by 4×10^6 equal-mass particles, giving a mass ratio $M_d : M_b = f_d : 1 - f_d = 0.8 : 0.2$. Further details of the setup methods used can be found in Debattista & Sellwood (2000).

In units where $R_d = M = G = 1$, which gives a unit of time $(R_d^3/GM)^{1/2}$, the values chosen for the various parameters are given in Table 2. This choice of parameters gives a flat rotation curve out to large radii, as shown in Fig. 1.

The simulation was run on a 3-D cylindrical polar grid code (described in Sellwood & Valluri [1997]) with $N_R \times N_\phi \times N_z = 60 \times 64 \times 225$. The radial spacing of grid cells increases logarithmically from the center, with the outer edge of the grid at just over $15R_d$. The vertical spacing of the grid planes, δz , was set to $0.0125R_d$. I used Fourier terms up to $m = 8$ in the potential, which was softened with the standard Plummer kernel, of softening length $\epsilon = 0.0125R_d$.

$t = 0$	
Halo core radius	$r_c = 5$
Halo circular velocity	$v_0 = 0.648$
Disc scaleheight	$z_d = 0.1$
Disc truncation radius	$R_t = 5$
Bulge truncation radius	$r_b = 0.78$
$t = 200$	
Bar semi-major axis	$a_B = 1.8 \pm 0.1$
Bar pattern speed	$\Omega_p = 0.296 \pm 0.011$
Bar speed parameter	$\mathcal{R} = 1.2 \pm 0.1$

Table 2. Parameter values of the N -body model.

Time integration was performed with a leapfrog integrator using a fixed time-step $\delta t = 0.02$.

The equilibrium set up using epicyclic theory is rather approximate at this high Q ; nonetheless, the system quickly relaxes to a new equilibrium close to the initial conditions. The resulting axisymmetric system is unstable and forms a rapidly rotating bar by $t = 150$. Fig. 2 shows the system at $t = 200$, the time I chose for this analysis; by this time, the bar had gone through a period of growth and Ω_p had settled to a well defined value. The bar is strong in the disc, with a weaker triaxiality in the bulge. The values of the bar's parameters at this time are given in Table 2. Note that the resulting N -body model of an SB0 galaxy is reasonable, with a bar which is neither too weak nor too strong, having a_B/R_d towards the upper limit of, but within, the range of the ADC sample.

Since the dark matter halo is frozen, Ω_p remains constant except for small oscillations produced by interference with weak spirals. I chose $t = 200$ because the spirals were relatively weak at this time, allowing me to measure Ω_p with a minimum of interference.

3.2 Pattern speed measurements

For TW measurements on the N -body system, I began with the disc in the xy -plane with the bar along the x -axis, as in Fig. 2. For an observer at positive z , viewing the system at an arbitrary orientation requires three rotations. Rotating the system (rather than the frame), the first rotation is about the z -axis through an angle ψ_{bar} , followed by a rotation about the x -axis to give an inclination i . At this point, the XY frame of the TW integrals is identical to the xy frame. A third rotation, through an angle δ_{PA} about the z -axis, introduces an error in PA_{disc} if the observer continues to identify (X, Y) with (x, y) . (Note that, in this definition, $\delta_{\text{PA}} > 0$ moves the assumed disc major-axis away from the bar's major-axis.) From here on, for notational convenience, I refer to the X and Y axes as the *assumed* major and minor axes of the system (*i.e.* the x and y axes), even when $\delta_{\text{PA}} \neq 0$. Fig. 3 shows an example of the system after such a series of rotations.

I measured \mathcal{X} and \mathcal{V} for $0^\circ \leq \psi_{\text{bar}} \leq 90^\circ$, $0^\circ \leq i \leq 90^\circ$ and $-90^\circ \leq \delta_{\text{PA}} \leq 90^\circ$ in 11 slits covering the region $-Y_{\text{max}} \leq Y \leq Y_{\text{max}}$. Here Y_{max} is $1.2 \times$ the largest of the projections onto the Y -axis of the bar's 3 principal axes. This limited range in Y mimics the typical observational setup,

and reduces the noise in the measurement. The values of \mathcal{X} and \mathcal{V} for each slit were obtained as:

$$\mathcal{X} = \frac{1}{\mathcal{P}} \sum_{i \in \text{slit}} w_i X_i, \quad \mathcal{V} = \frac{1}{\mathcal{P}} \sum_{i \in \text{slit}} w_i V_{z,i}, \quad (6)$$

where $V_{z,i}$ and X_i are the line-of-sight velocity and X coordinate of particle i , w_i is the weight assigned to each particle and $\mathcal{P} = \sum_{i \in \text{slit}} w_i$ (which corresponds to $h(Y) = 1/\int \Sigma dX$, so that \mathcal{X} and \mathcal{V} are the luminosity-weighted average position and velocity of each slit, as in observations). Except where noted, I used $w_i = 1$ for all particles, whether disc or bulge; thus $\mathcal{P} = N_{\text{slit}}$, the number of particles in the slit. If $\mathcal{X}(X_{\text{max}})$ and $\mathcal{V}(X_{\text{max}})$ represent the integrals extending from $-X_{\text{max}}$ to X_{max} , then error estimates $\sigma_{\mathcal{X}}$ and $\sigma_{\mathcal{V}}$ were obtained by considering their maximum variation with X_{max} outside the bar radius. Because the number of particles in each slit was high, these radial variations are due only to weak non-axisymmetric structure at large radius. In Fig. 4, I show $\mathcal{X}(X_{\text{max}})$ and $\mathcal{V}(X_{\text{max}})$ for a typical slit.

To measure the pattern speed from a set of such slits, I fit a straight line to \mathcal{V} as a function of \mathcal{X} , as in observations, using least-squares weights W_{slit} . The principal observational uncertainty is in \mathcal{V} and is due to photon statistics; I therefore used $W_{\text{slit}} = (\sigma_{\mathcal{V}}/\sqrt{N_{\text{slit}}})^{-2}$.

The slope of this fitted line is $\Omega_{\text{TW}} \sin i$, where I use the notation Ω_{TW} to distinguish from the pattern speed measured through the time evolution. An example of such a fit is shown in Fig. 5, which reveals that $|\mathcal{X}|$ and $|\mathcal{V}|$ increase with increasing $|Y|$, until they reach a maximum, and then decrease. Observational requirements of high S/N in modest time usually restricts slit offsets to ones at, or inside, the maximum in $|\mathcal{X}|$ (*e.g.* Aguerri et al. 2003).

I verified that the TW method accurately measures Ω_p when $\delta_{\text{PA}} = 0$: in the range $10^\circ \leq i \leq 80^\circ$ and $10^\circ \leq \psi_{\text{bar}} \leq 80^\circ$, fractional errors, $|\Delta\Omega/\Omega_p| \equiv |(\Omega_{\text{TW}} - \Omega_p)/\Omega_p|$, are smaller than 20 per cent, in agreement with Tremaine & Weinberg (1984).

Besides this experiment, I tried various others. For example, in two experiments, I set $w_i = 0$ and $w_i = 2$ for the bulge particles, leaving $w_i = 1$ for the disc ones. The results were consistent with those presented above, leading me to conclude that any plausible difference between the stellar mass-to-light ratio of the bulge and disc does not introduce large errors in Ω_{TW} .

4 SIMPLE PA_{disc} ERRORS

4.1 Sensitivity to errors in PA_{disc}

Fig. 4 also plots $\mathcal{X}(X_{\text{max}})$ and $\mathcal{V}(X_{\text{max}})$ for $\delta_{\text{PA}} = \pm 5^\circ$. It is clear that these small errors in PA_{disc} change the values of $\mathcal{X}(X_{\text{max}})$ and $\mathcal{V}(X_{\text{max}})$ substantially, while qualitatively looking similar to the $\delta_{\text{PA}} = 0$ case. Moreover, these changes are at all X_{max} , particularly in the case of $\mathcal{V}(X_{\text{max}})$; thus, limiting the integrals to small X_{max} does not diminish the error (although it does not increase it, either, unless X_{max} is well within the bar). For this one slit, these changes gave an Ω_{TW} which is in error by up to 100 per cent.

In Fig. 6, I again plot the integrals as a function of Y , but this time for $\delta_{\text{PA}} = \pm 5^\circ$. Both $|\mathcal{X}|$ and $|\mathcal{V}|$ reach a smaller (larger) maximum in the case of $\delta_{\text{PA}} = -5^\circ$ (δ_{PA}

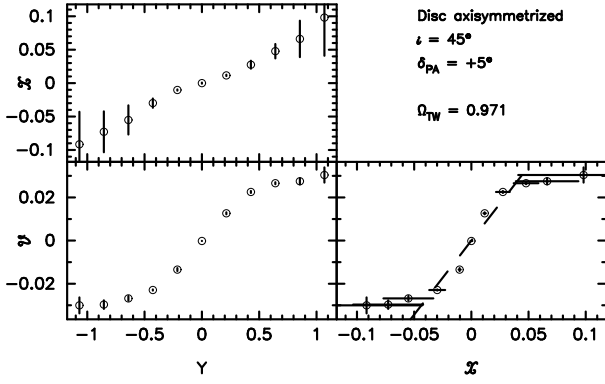


Figure 7. As in Fig. 5 but for $\delta_{PA} = +5^\circ$ with the disc axisymmetrized by shuffling the particles in azimuth. The pattern speed fit in the right panel is, therefore, merely an artifact.

$= +5^\circ$), while at larger offsets, the decrease in the values of the integrals is faster (slower) than in the $\delta_{PA} = 0$ case; for $\delta_{PA} = -5^\circ$, \mathcal{V} even switches sign.

To begin to understand these changes, I consider an axisymmetric system. For a slit at $Y > 0$, when $\delta_{PA} = 0$, the contribution to \mathcal{X} and \mathcal{V} from $-X$ is exactly cancelled by that from $+X$. When $\delta_{PA} > 0$, several changes occur. First, $+X$ is always closer to the galaxy center (in the disc's own plane), and at a smaller angle from the intrinsic major-axis, than is $-X$. Therefore $|V_{los}(+X)| > |V_{los}(-X)|$, if the rotation curve is flat, giving \mathcal{V} a positive perturbation, which is further enhanced if the density profile of the disc decreases radially, as is generally the case. The changes in \mathcal{X} are due solely to the radial variation of the surface density; when this is constant everywhere, \mathcal{X} is exactly zero at all δ_{PA} . Conversely, an exponential disc with small scale-length (relative to the slit offset) gives large values of \mathcal{X} when $\delta_{PA} \neq 0$. The change in \mathcal{V} is large already at small X_{max} (see Fig. 4), whereas the changes in \mathcal{X} are more distributed over X_{max} . This behavior is due to the fact that the integrand ΣV_{los} grows more rapidly with X than does ΣX . Indeed, for a flat rotation curve $|V_{los}(X) + V_{los}(-X)|$ is largest at $X = 0$.

Fig. 7 plots \mathcal{X} and \mathcal{V} at $\delta_{PA} = +5^\circ$ for the axisymmetric disc produced by randomizing the azimuthal coordinate of all the particles in the N -body model (preserving the average radial density profile). Even in the absence of any non-axisymmetric structure, misaligned slits produce non-zero \mathcal{X} and \mathcal{V} , which may plausibly be fit to a pattern speed where none is present.

These extra contributions to \mathcal{X} and \mathcal{V} will still be present in the barred case, modified by the presence of the bar (*e.g.* \mathcal{X} will still change even when the azimuthally averaged radial profile is constant, and \mathcal{X} changes sign if the bar crosses the Y -axis), but fundamentally of the same character. It is then easy to imagine that some combination of Fig. 5 and Fig. 7 produces the bottom panels of Fig. 6, at least qualitatively. For $\delta_{PA} = -5^\circ$, the signs of \mathcal{X} and \mathcal{V} in Fig. 7 would be reversed, which then combines with Fig. 5 to produce something like the top panels of Fig. 6.

Fig. 6 suggests that, when $\delta_{PA} < 0$, it may be possible to recognize $\delta_{PA} \neq 0$ by the large χ^2 in the linear regression. Unfortunately the most discrepant points are the ones at large offset; in observations, their σ_V will certainly be (fractionally) much larger than here, in which case χ^2 is not

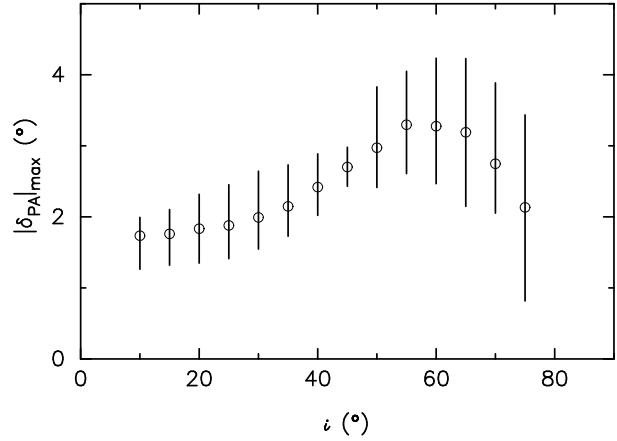


Figure 8. The maximum permitted error in PA_{disc} required for Ω_{TW} accurate to 30 per cent. These have been computed in the range $15^\circ \leq \psi_{bar} \leq 75^\circ$, with circles representing the averages and the error bars indicating the extreme cases.

likely to be greatly increased by these points. Moreover, the two most discrepant points are at small $|\mathcal{X}|$ and are thus unlikely to have been chosen for observation in the first place. It therefore seems likely that, in the absence of considerable investment in telescope time (which anyway would not catch $\delta_{PA} > 0$), the error in PA_{disc} would go unnoticed.

The 5° errors of Fig. 6 give errors in Ω_{TW} as large as 48 per cent. In Fig. 8, I present the largest errors permitted to guarantee Ω_{TW} accurate to 30 per cent. The limits on δ_{PA} are quite stringent: $|\delta_{PA}| \leq 4^\circ$ is needed at $i = 60^\circ$ and the limit is smaller at other inclinations. (Note, however, that for $|\Delta\Omega/\Omega_p|$ to be larger than 30 per cent, it is necessary, *but not sufficient* for $|\delta_{PA}|$ to be larger than the values given in Fig. 8, since δ_{PA} can be either positive or negative.)

4.2 Scatter from random PA_{disc} errors

Fig. 9 plots $\Delta\Omega/\Omega_p$ and $\mathcal{R}_{TW} \equiv (\Omega_p/\Omega_{TW})\mathcal{R}$ as functions of δ_{PA} . (This definition of \mathcal{R}_{TW} ignores the errors in V_c and a_B due to δ_{PA} . These errors change \mathcal{R}_{TW} by only a small amount for the inclinations of interest here.) The shaded region in the bottom panel indicates the region of fast bars; it is clear that once $|\delta_{PA}|$ becomes larger than about 2° , values of \mathcal{R}_{TW} scatter outside this region. Uncertainties in PA_{disc} must therefore also contribute to the scatter in measurements of \mathcal{R} . Assuming Gaussian errors in PA_{disc} with zero mean and FWHM of 5° (2°), I found a scatter in \mathcal{R}_{TW} , $\Delta\mathcal{R}_{\delta}$, (defined as the 67 per cent interval about the median), of $\Delta\mathcal{R}_{\delta} \simeq 0.4$ ($\Delta\mathcal{R}_{\delta} \simeq 0.2$), as shown in Fig. 10; this is substantially larger than the intrinsic measurement scatter at $\delta_{PA} = 0$, which is only $\Delta\mathcal{R} \simeq 0.06$. Since, for the ADC sample, the observational root-mean-square uncertainty in PA_{disc} is 2:1, measurements of \mathcal{R} with the TW method cannot directly resolve the intrinsic distribution of \mathcal{R} if it is as narrow as hydrodynamical simulations require, even before other sources of scatter are considered.

An important characteristic of the scatter is that $\mathcal{R}_{TW} < 1$ may result. Since $\mathcal{R} < 1$ is physically impossible (Contopoulos 1980), this may help in distinguishing the effects of PA_{disc} errors from the intrinsic distribution of \mathcal{R} .

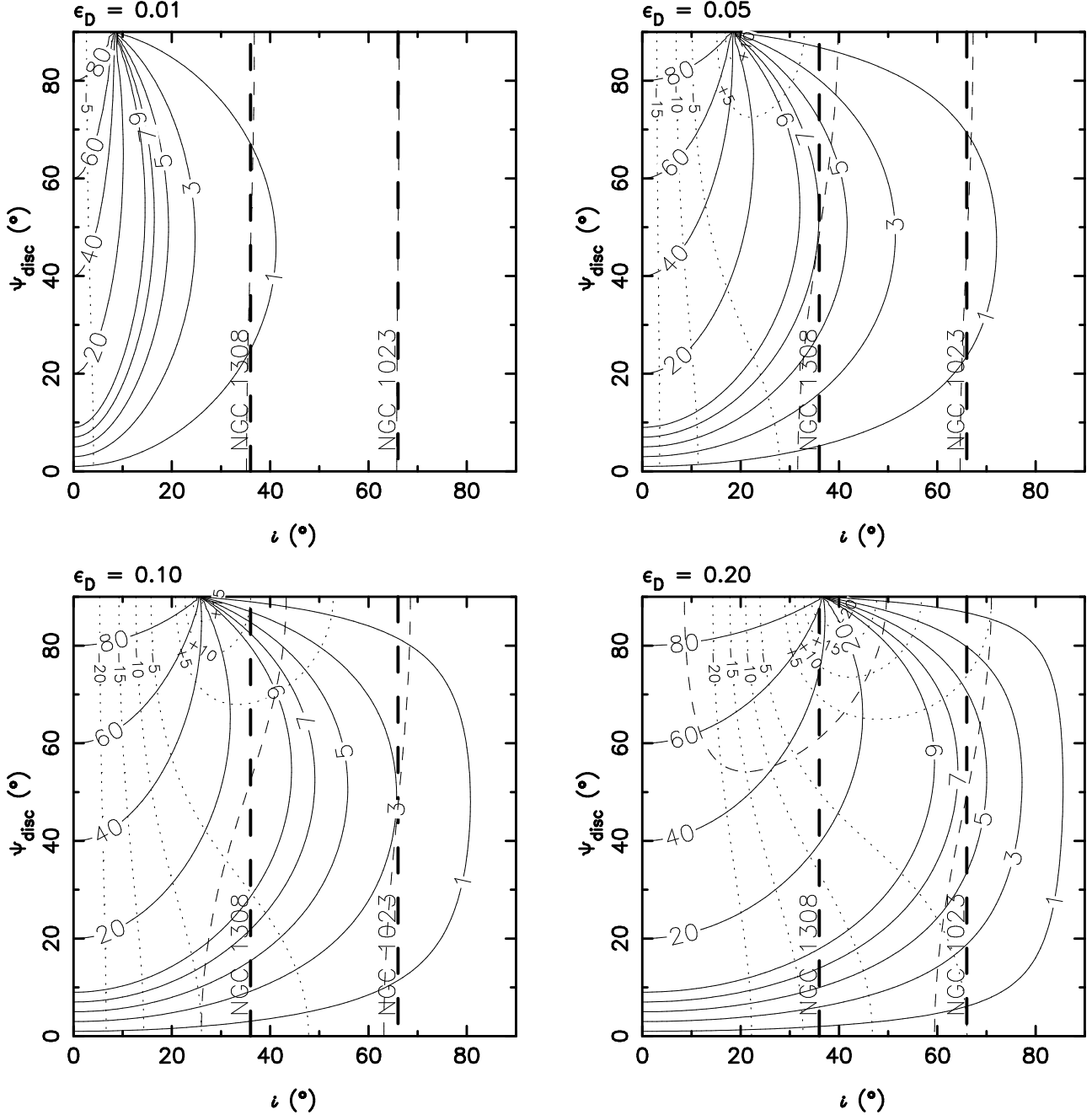


Figure 11. Contours of the errors in PA_{disc} and i resulting from assuming that an intrinsically elliptical disc is circular. The disc ellipticity, ϵ_D , in each case is indicated in the top-left corner of each panel. The solid contours show the errors in PA_{disc} , while the dotted contours show the errors in i . Each contour is labelled by the error it corresponds to; these are positive only for PA_{disc} , because this figure only considers $\psi_{\text{disc}} > 0$, for the sake of simplicity. For large inclinations (near edge-on), only very small errors in PA_{disc} result, but as the disc becomes closer to face on, the errors generally become larger. The dashed lines indicate the 2 galaxies on which the TW method has been used with the smallest (NGC 1308) and largest (NGC 1023) apparent inclination: the bold dashed lines are the inclinations assumed by the corresponding authors (see Table 1), which were obtained by assuming the outer disk is circular, while the thin dashed lines indicate the loci of $\epsilon_{\text{app}} = 1 - \cos i_{\text{app}}$. Where $\epsilon_D > 1 - \cos i$ (e.g. NGC 1308 when $\epsilon_D = 0.2$), the typical errors in i and, especially, in PA_{disc} become very large, up to 90° .

5 ADDITIONAL NON-AXISYMMETRIES

If the disc contains additional non-axisymmetric structure besides the bar, then this will interfere with the measurement of Ω_p . If the disc non-axisymmetric density can be decomposed into 2 components, with different pattern speeds,

then Ω_{TW} is a luminosity and asymmetry weighted average of the two pattern speeds (Debattista et al. 2002b). I assume that the second component is a weaker non-axisymmetric structure and/or is at larger radius and therefore lower surface brightness, so that this type of interference will be relatively small and can be ignored. (This can also be justified

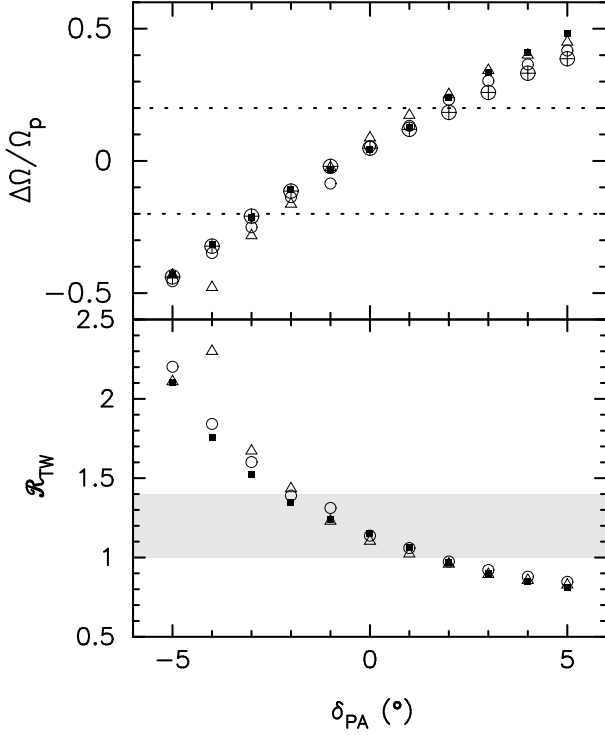


Figure 9. The variation of $\Delta\Omega/\Omega_p$ (top) and \mathcal{R}_{TW} (bottom) for small errors in PA_{disc} , at $i = 45^\circ$. Circles, triangles and filled squares are for $\psi_{\text{bar}} = 30^\circ, 45^\circ$ and 60° respectively. The dotted lines in the top panel represent errors of 20 per cent, while in the bottom panel, the shaded region indicates $1.0 \leq \mathcal{R}_{\text{TW}} \leq 1.4$. The crossed open circles in the top panel represent a system with i and ψ_{bar} as in NGC 7079.

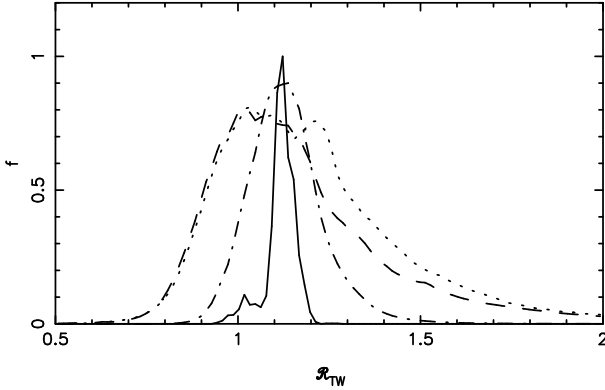


Figure 10. The distribution of \mathcal{R}_{TW} for various distributions of random errors in PA_{disc} . The solid line shows the distribution without PA_{disc} errors, while the dot-dashed and dashed lines show the distributions resulting from Gaussian errors of zero mean and $\text{FWHM} = 2^\circ$ and 5° , respectively. The dotted line is also for Gaussian errors with $\text{FWHM} = 5^\circ$, but uses $W_{\text{slit}} = \sigma_V^{-2}$ to measure Ω_{TW} . Each line has been rescaled vertically for clarity. The distributions represent averages over $30^\circ \leq i \leq 70^\circ$ and $10^\circ \leq \psi_{\text{bar}} \leq 80^\circ$, and are not substantially changed by modest changes to these limits.

by noting that the weak spiral structure at large radius in the N -body model does not introduce substantial errors in Ω_{TW} .) Instead, I concentrate only on the effect these secondary non-axisymmetric structures have on Ω_{TW} due to the errors they introduce in the measurement of PA_{disc} .

5.1 Elliptical discs

In all cases in which the TW method has been used, PA_{disc} has been measured from surface photometry under the assumption that the disc is intrinsically circular. When the disc is elliptical, deprojecting with this assumption gives rise to errors in i and PA_{disc} , as shown in Fig. 11. These errors lead to further scatter in \mathcal{R}_{TW} .

To study this scatter, I assumed that, at large radii, ϵ_D and ψ_{disc} (where ψ_{disc} is the angle of the elliptical disc in the plane of the disc relative to the line-of-nodes) are both constant, and computed the apparent PA_{disc} (PA_{app}) and apparent i (i_{app}) resulting from the assumption of a circular disc. I used these to measure the apparent circular velocity ($V_{c,\text{app}}$) and bar semi-major axis ($a_{B,\text{app}}$). I then obtained $\Omega_{\text{TW}} \sin i_{\text{app}}$ as the slope of the best-fitting line to $(\mathcal{X}, \mathcal{Y})$, from which I measured $\mathcal{R}_{\text{TW}} = V_{c,\text{app}} / (a_{B,\text{app}} \Omega_{\text{TW}})$. By assuming that the bar is infinitely narrow, I measured the apparent bar PA in the disc plane, $\psi_{b,\text{app}}$, and then averaged \mathcal{R}_{TW} over $30^\circ \leq i_{\text{app}} \leq 70^\circ$, $10^\circ \leq \psi_{b,\text{app}} \leq 80^\circ$ and $-90^\circ < \psi_{\text{disc}} \leq 90^\circ$. Fig. 12 plots the resulting distributions of \mathcal{R}_{TW} obtained for various constant ϵ_D . The ellipticity-induced scatter, $\Delta_{\mathcal{R},\epsilon}$, grows rapidly with ϵ_D ($\Delta_{\mathcal{R},\epsilon} \simeq 0.2, 0.6$ and 0.9 for $\epsilon_D = 0.01, 0.05$ and 0.1 respectively), with most measurements of \mathcal{R}_{TW} outside the range $1.0 \leq \mathcal{R}_{\text{TW}} \leq 1.4$ once $\epsilon_D = 0.1$. The distinctive peak to $\mathcal{R}_{\text{TW}} < 1$ for the larger values of ϵ_D is due to the fact that the distribution of δ_{PA} , at fixed i_{app} , has peaks near $\max(|\delta_{\text{PA}}|)$. The peak at $\mathcal{R}_{\text{TW}} < 1$ is higher than that at $\mathcal{R}_{\text{TW}} > 1$ because $\mathcal{R} \propto \Omega_p^{-1}$.

Fig. 12 also shows the distribution of \mathcal{R}_{TW} resulting from the ellipticity distribution of Andersen & Bershadsky (2002) for later-type unbarred galaxies. The two largest values of ϵ_D in their sample of 28 were $\epsilon_D = 0.232^{+0.070}_{-0.064}$ and $\epsilon_D = 0.165 \pm 0.083$ (Andersen 2002, private communication). As can be seen in Fig. 11, large values of ϵ_D produce PA_{disc} errors as large as 90° in the (apparent) inclination range of interest, which would result in very large errors in Ω_{TW} . Therefore I truncated their distribution at $\epsilon_D = 0.1$ and 0.15 . The resulting scatter is $\Delta_{\mathcal{R},\epsilon} \simeq 0.5$ and $\simeq 0.6$ respectively.

To compute an upper limit for the characteristic ϵ_D of SB0 galaxies, I define P_f as the probability that all measurements will result in $0.5 < \mathcal{R}_{\text{TW}} < 2.5$, a range outside which, at the 67 per cent interval, none of the measurements of Table 1 fall. Then, for that sample, I compute P_f by matching i_{app} and $\psi_{b,\text{app}}$ to the observed values and averaging over ψ_{disc} , obtaining Fig. 13. The probability of having found \mathcal{R}_{TW} less than 0.5 or greater than 2.5 for one or more of these galaxies exceeds 90 per cent (75 per cent for $\mathcal{R}_{\text{TW}} > 5.0$) if $\epsilon_D \geq 0.07$ for all of them. (The strongest constraints come from the low inclination galaxies, while NGC 1023, which has the largest inclination of this sample, does not constrain ϵ_D at all, up to 0.1.) This upper limit on the disc ellipticity is in rough agreement with previous measurements (*e.g.* Franx & de Zeeuw 1992) for unbarred galaxies.

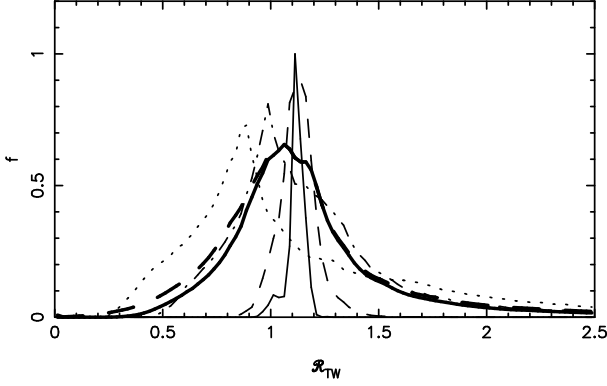


Figure 12. The distribution of \mathcal{R}_{TW} resulting from elliptical discs. The thin solid line shows the intrinsic distribution when $\epsilon_D = 0$, while the thin dashed, dot-dashed and dotted lines show the distributions resulting from errors caused by $\epsilon_D = 0.01, 0.05$ and 0.1 , respectively. The thick solid and dashed lines are based on the empirical distribution of Andersen & Bershadsky, with a maximum ϵ_D of 0.1 and 0.15 respectively. Each line has been rescaled vertically for clarity. The distributions represent averages over $30^\circ \leq i_{\text{app}} \leq 70^\circ$ and $10^\circ \leq \psi_{b,\text{app}} \leq 80^\circ$, and are not substantially changed by modest changes to these limits.

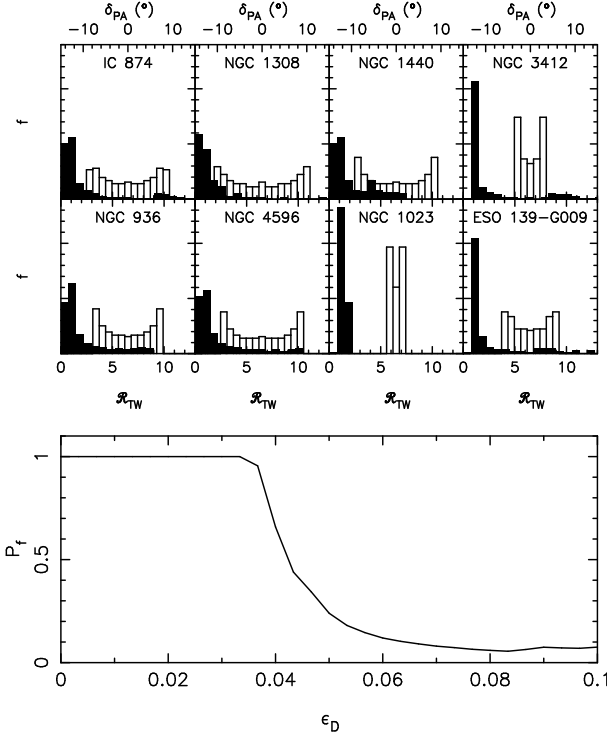


Figure 13. The bottom panel plots the probability, P_f , that none of the 8 galaxies of Table 1 is outside the range $0.5 \leq \mathcal{R}_{\text{TW}} \leq 2.5$ for ϵ_D fixed for all galaxies. The top 8 panels show the distributions of \mathcal{R}_{TW} (filled histograms and bottom scale) and δ_{PA} (open histograms, top scale) produced by matching $\psi_{b,\text{app}}$ and i_{app} for the galaxies in Table 1 under the assumption that $\epsilon_D = 0.07$ (where $P_f < 0.1$).

5.2 Rings

In Section 5.1, I assumed that ψ_{disc} is uncorrelated with ψ_{bar} . Correlations between ψ_{disc} and ψ_{bar} may be introduced by the outer rings often seen in SB galaxies. Two main types of outer rings are possible (*e.g.* Buta 1995): R_1 , which are aligned perpendicular to the bar, and R_2 , which line up with the bar. Galaxies selected for TW measurement do not contain strong rings, but conceivably weak rings might have been overlooked. To consider their effect on TW measurements, I simply set $\psi_{\text{bar}} = \psi_{\text{disc}}$ (for rings of type R_2) and $\psi_{\text{bar}} = \psi_{\text{disc}} + 90^\circ$ (for rings of type R_1) and proceeded as for Fig. 12. The results, unsurprisingly, showed that rings of type R_2 , which lead to $\delta_{\text{PA}} \leq 0$, produce $\mathcal{R}_{\text{TW}} \leq \mathcal{R}$, while rings of type R_1 lead to $\mathcal{R}_{\text{TW}} \geq \mathcal{R}$. Buta (1995) found mean ϵ_D of 0.26 and 0.13 for rings of type R_1 and R_2 respectively. If such rings had been present in the sample of Table 1, then the scatter in \mathcal{R}_{TW} would have been significantly higher.

5.3 Spirals

Recently, Barnes & Sellwood (2003) have questioned the interpretation of discrepancies between photometric and kinematic inclinations and PA's as resulting from disc ellipticities. Instead, they found evidence that spirals, or similar non-axisymmetries, produce these discrepancies. They reported an average PA_{disc} uncertainty of about 4° for earlier-type galaxies.

PA_{disc} errors of this type will produce scatter in \mathcal{R}_{TW} in much the same way as do random PA_{disc} errors. For $\sigma \simeq 4^\circ$, I found a resulting scatter $\Delta \mathcal{R}_{\text{spr}} \simeq 0.7$. However, the sample of galaxies used by Barnes & Sellwood (taken from Palunas & Williams [2000]), excluded galaxies as early as S0, so this value is somewhat uncertain and is probably an over-estimate.

5.4 Warps

While most disc galaxies are coplanar inside R_{25} (Briggs 1990), examples of warps inside this radius are not unknown. One extreme case is the interacting galaxy NGC 3718, which has a warp of about 80° at R_{25} (Schwarz 1985). However, such strongly interacting galaxies are usually not selected for TW studies. Furthermore, the large velocity dispersions of early-type galaxies serve to stiffen their stellar discs (De-battista & Sellwood 1999), so that any warps inside R_{25} are generally small. Therefore warps probably do not introduce significant scatter in TW measurements.

6 DISCUSSION AND CONCLUSIONS

6.1 How realistic are the error estimates?

How realistic are these estimates of $\Delta\Omega/\Omega_p$ and the $\Delta\mathcal{R}$'s? Since, for $\delta_{\text{PA}} < 0$, the values of \mathcal{X} and \mathcal{V} are not all close to a straight line (see Fig. 6), a poor choice of W_{slit} could lead to excess scatter. At $\delta_{\text{PA}} = 0$, I obtained the smallest $|\Delta\Omega/\Omega_p|$ with $W_{\text{slit}} = \sigma_{\mathcal{V}}^{-2}$, which is defined only from the variations of \mathcal{V} with X_{max} . This is unsurprising, since $\sigma_{\mathcal{V}}$ represents the full uncertainty in \mathcal{V} . All other definitions of W_{slit} produced larger errors. In particular, while $W_{\text{slit}} = \sigma_{\mathcal{V}}^{-2}$ gives a mean

$\Delta\Omega/\Omega_p$ of 3 per cent, $W_{\text{slit}} = (\sigma_V/\sqrt{N_{\text{slit}}})^{-2}$ produces a mean $\Delta\Omega/\Omega_p$ of 7 per cent.

However, when $\delta_{\text{PA}} \neq 0$, W_{slit} favoring slits with small offset, which generally acquire fractionally smaller perturbations, produces smaller scatter. Fig. 10 compares the distributions of \mathcal{R}_{TW} from random Gaussian PA_{disc} errors of $\text{FWHM} = 5^\circ$ as obtained using $W_{\text{slit}} = (\sigma_V/\sqrt{N_{\text{slit}}})^{-2}$ and $W_{\text{slit}} = \sigma_V^{-2}$. The former produces a smaller scatter, due mostly to the reduced noise at $\mathcal{R}_{\text{TW}} > \mathcal{R}$, *i.e.* at $\delta_{\text{PA}} < 0$. I tried other definitions of W_{slit} , including $\sigma_{\mathcal{R}}^{-2}$, equal weights, \mathcal{P} , and various combinations of these. I also tried using only 3 slits (the central one and either the two with the largest $|\mathcal{R}|$ or the two flanking slits), as is often done in observations. These always gave larger scatter, typically by 20 per cent or more. I therefore used $W_{\text{slit}} = (\sigma_V/\sqrt{N_{\text{slit}}})^{-2}$ everywhere in this paper to compute $\Delta\Omega/\Omega_p$ and the $\Delta\mathcal{R}$'s. Thus I am assured of a conservative estimate of the scatter, while also matching better the main source of noise in the observations: the photon statistics.

Since I have used only one simulation to estimate the scatter, I need to show that this simulation does not overestimate the errors in Ω_{TW} that real galaxies would suffer. Perhaps the most important parameter affecting the size of the scatter in Ω_{TW} is a_B/R_d , as described in Section 2. A series of experiments with razor-thin, flat rotation curve, axisymmetric exponential discs showed that, indeed, the scatter in Ω_{TW} due to random PA_{disc} errors increases as R_d decreases. Since my model SB0 has a value of a_B/R_d that is towards the upper end of those in the ADC sample, my measurements of $\Delta_{\mathcal{R},\delta}$ and $\Delta_{\mathcal{R},\epsilon}$ probably underestimate somewhat the scatter which the same PA_{disc} errors would produce in real galaxies. The same conclusion resulted from a test with a lower quality (102K particle) simulation having a larger bar ($a_B/R_d = 2.6$); for random Gaussian errors of $\text{FWHM} = 5^\circ$, this bar produced $\Delta_{\mathcal{R},\delta} = 0.3$ versus 0.4 for the shorter bar used in this paper.

The trend with δ_{PA} seen in Fig. 6 is in the same sense as was found by Debattista & Williams (2002) for NGC 7079. Fig. 9 plots $\Delta\Omega/\Omega_p$ for the same projection as NGC 7079. The errors in Ω_{TW} due to δ_{PA} for NGC 7079 ($a_B/R_d = 1.5 \pm 0.2$) reported by Debattista & Williams are perhaps a little larger than those computed here. Gratifyingly, the error estimates produced by the N -body model are not unrealistically large.

6.2 The ellipticity of early-type barred galaxies

The ellipticities of S0 galaxies are poorly constrained. From photometry only, Fasano et al. (1993) found that they could not rule out that they are perfectly oblate. The two S0 galaxies with directly measured ellipticities, IC 2006 (Franx et al. 1994) and NGC 7742 (Rix & Zaritsky 1995) both have small, possibly zero, ellipticity ($\epsilon_\Phi = 0.012 \pm 0.026$ and 0.02 ± 0.01 respectively). The ellipticities of SB galaxies are not much better constrained, undoubtedly because they require a distinction between the inner, bar-dominated, region and the outer parts. Photometry alone, therefore, is of limited use, and kinematics also are needed. Unfortunately, most TF studies have avoided SB galaxies. Debattista & Sellwood (2000) showed that the small fraction of bright ($M_I \leq -21$) SB galaxies contaminating the sample of Mathewson & Ford (1996), who selected against SB galaxies, satisfies the same

TF relation, and has the same scatter, as the unbarred (SA) galaxies. Sakai et al. (2000) calibrated the TF relation of nearby galaxies with Cepheid distances; their sample of 21 galaxies contained a more representative fraction of SB galaxies, at ~ 30 per cent. The resulting TF relation, including the scatter, also was identical for SA and SB galaxies. Thus we may suppose that the TF-based constraint of Franx & de Zeeuw (1992), $\epsilon_\Phi < 0.1$, also holds for SB galaxies.

The constraint obtained here, $\epsilon_D \lesssim 0.07$, is in rough agreement with the constraints for SA galaxies. However, an important possible bias needs to be pointed out. The ADC sample of 6 galaxies explicitly excluded galaxies for which, at large radius, the observed PA_{disc} changes substantially with radius. From a sample of 11 galaxies for which they obtained surface photometry, one (Aguerre 2002, private communication) was excluded for this reason. If either ϵ_D or ψ_{disc} changes with radius, then the observed changes in PA_{disc} will typically be greater in galaxies with larger mean ϵ_D . Thus the cut on the size of PA_{disc} variations may have introduced a bias in the ellipticity distribution of the ADC sample; on the other hand, large variations in PA_{disc} may have been caused instead by spirals or by a warp.

Although these constraints on SB galaxy ellipticities are consistent with the constraints on SA galaxy ellipticities, this does not mean that their ellipticity distributions are the same, since both the TF and the TW constraint obtain only upper limits on ϵ_D .

6.3 The intrinsic distribution of \mathcal{R}

Hydrodynamical simulations of SB galaxies find a narrow range of $\mathcal{R} = 1.2 \pm 0.2$. The presently observed distribution of \mathcal{R}_{TW} is dominated by the observational uncertainties in Ω_{TW} , a_B and V_c . Nevertheless, it is clear that all 8 galaxies measured so far are consistent with the range found in hydrodynamical simulations. In their N -body simulations with cosmologically motivated initial conditions, Valenzuela & Klypin (2002) found that bars with $\mathcal{R} = 1.7$ were produced, which they considered to be consistent with the observations. Indeed, for 4 of the 8 galaxies listed in Table 1, $\mathcal{R} = 1.7$ is within the error interval. However, 3 of these 4 galaxies are the ones with the largest error bars, and the fourth galaxy is only just barely consistent with this value. For the ADC sample, which have well-determined PA_{disc} uncertainties, the root-mean-square uncertainty in PA_{disc} is 2:1. From the results of Section 2, the corresponding scatter in \mathcal{R}_{TW} , excluding any contribution due to disc ellipticity, should be $\Delta_{\mathcal{R},\delta} \simeq 0.4$. Allowing for this scatter, it seems possible that 1.7 is outside the intrinsic range of \mathcal{R} .

For a crude estimate of the intrinsic range of \mathcal{R} , suppose we can write $\Delta_{\mathcal{R},\text{obs}}^2 = \Delta_{\mathcal{R},\text{int}}^2 + \Delta_{\mathcal{R},\delta}^2 + \Delta_{\mathcal{R},\epsilon}^2 + \Delta_{\mathcal{R},\text{unc}}^2$, where $\Delta_{\mathcal{R},\text{obs}}$ is the observed scatter, $\Delta_{\mathcal{R},\text{int}}$ is the intrinsic range of \mathcal{R} , $\Delta_{\mathcal{R},\delta}$ is the scatter due to random PA_{disc} errors, $\Delta_{\mathcal{R},\epsilon}$ is the scatter due to disc ellipticity and $\Delta_{\mathcal{R},\text{unc}}$ is the scatter induced by uncertainties in the measurements of Ω_p , a_B and V_c . All these $\Delta\mathcal{R}$'s are assumed to be 67 per cent intervals. (Other sources of scatter, such as direct interference from spiral or other structure, small errors in slit orientation, *etc.*, may be present but are assumed here to be unimportant.) From Section 2 I get that $\Delta_{\mathcal{R},\text{obs}} \simeq 1.0$ and $\Delta_{\mathcal{R},\text{unc}} \simeq 0.7$, while from Section 4 I get $\Delta_{\mathcal{R},\delta} \simeq 0.4$. If $\epsilon_D = 0$ for all galaxies, then $\Delta_{\mathcal{R},\text{int}} \simeq 0.6$, while the distri-

bution of ϵ_D of Andersen & Bershadsky (2002), truncated at $\epsilon_D = 0.1$, produces $\Delta\mathcal{R}_{int} \simeq 0.3$. If, on the other hand, the interpretation of Barnes & Sellwood (2003) is correct, then $\Delta\mathcal{R}_{\epsilon} = 0$, but it is replaced by $\Delta\mathcal{R}_{spr} \lesssim 0.7$. It therefore seems possible that the intrinsic range of \mathcal{R} for early-type galaxies spans a range similar to the later-type galaxies.

Unfortunately, the sample size is still too small for a proper statistical test of this suggestion. If correct, then the fact that SB galaxies have the same distribution of \mathcal{R} as the more gas-rich later-type SB galaxies requires that gas is not dynamically very important for the evolution of Ω_p .

6.4 Future work and conclusions

The current sample of TW measurements is still quite small, so it is not unlikely that, in the future, more measurements will be obtained. The results of this paper can be read as an endorsement of careful surface photometry of target galaxies to accurately measure PA_{disc} . Inclinations in the range $50^\circ \leq i \leq 60^\circ$ are preferable, since they are less sensitive to errors in PA_{disc} . For statistical studies, especially to constrain the distribution of \mathcal{R} , it would be very useful if future studies were to report their uncertainty in PA_{disc} . Galaxies with strong outer rings do not make good candidates for TW measurement because of the inherent uncertainty in PA_{disc} , and should be avoided. If the TW method is ever to be used on late-type galaxies, perhaps in the infra-red (*e.g.* Baker et al. 2001), care must be taken that the presence of spirals does not lead to excess errors in PA_{disc} .

The pattern speed of triaxial elliptical galaxies is a matter of theoretical speculation. Because of the large velocity dispersions and low stellar streaming velocities, it is generally thought that their pattern speeds must be small. Measurement of their pattern speeds would be very interesting, but unfortunately, application of the TW method to elliptical galaxies is likely to be accompanied by significant uncertainty in their intrinsic orientations (amongst other difficulties). Thus TW measurements of their pattern speeds may have large uncertainties.

I have shown that errors in PA_{disc} lead to significant error in TW measurements. For the observational level of random Gaussian errors, the resulting scatter in \mathcal{R} is $\Delta\mathcal{R}_{\delta} \simeq 0.4$. If barred galaxies are also modestly elliptical, then the total scatter increases further, depending on the distribution of ϵ_D . Given the observed range of \mathcal{R} , this suggests, therefore, that the gas-poor early-type galaxies have a narrow distribution of $\mathcal{R} \sim 1.0-1.4$, not much different from gas-rich late-type galaxies, as determined by independent means. This result would imply that gas is not dynamically important for the evolution of bar pattern speeds.

Acknowledgments.

This work has been made possible by support from the Schweizerischer Nationalfonds through grant 20-64856.01. I thank Enrico Maria Corsini, Joris Gerssen, Dave Andersen, Jerry Sellwood, Alfonso Aguerri and Niranjan Sambhus for comments and discussion.

REFERENCES

- Aguerrri J. A. L., Debattista V. P., Corsini E. M., 2003, MNRAS, 338, 465
- Andersen D. R., Bershadsky M. A., Sparke L. S., Gallagher J. S., Wilcots E. M., 2001, ApJ, 551, L131
- Andersen D. R., Bershadsky M. A., 2002, in E. Athanassoula, A. Bosma & R. Mújica, eds, ASP Conf. Ser. Vol. 275, Disks of Galaxies: Kinematics, Dynamics and Perturbations. Astron. Soc. Pac., San Francisco, pg. 39
- Athanassoula E., 1992, MNRAS, 259, 345
- Baker A. J., Schinnerer E., Scoville N. Z., Englmaier P. P., Tacconi L. J., Tacconi-Garman L. E., Thatte N., 2001, in J. H. Knapen, J. E. Beckman, I. Shlosman & T. J. Mahoney, eds, ASP Conf. Ser. Vol. 249, The Central Kiloparsec of Starbursts and AGN: The La Palma Connection. Astron. Soc. Pac., San Francisco, pg. 78.
- Barnes I. C., Sellwood, J. A., 2003, AJ, 125, 1164
- Beauvais C., Bothun G., 1999, ApJS, 125, 99
- Binney J., de Vaucouleurs G., 1981, MNRAS, 194, 679
- Briggs F. H., 1990, ApJ, 352, 15
- Buta R., 1995, ApJS, 96, 39
- Contopoulos G., 1980, A&A, 81, 198
- Debattista V. P., Sellwood J. A., 1998, ApJ, 493, L5
- Debattista V. P., Sellwood J. A., 1999, ApJ, 513, L107
- Debattista V. P., Sellwood J. A., 2000, ApJ, 543, 704
- Debattista V. P., Corsini E. M., Aguerri J. A. L., 2002a, MNRAS, 332, 65
- Debattista V. P., Gerhard O., Sevenster M. N., 2002b, MNRAS, 334, 355
- England M. N., Gottesman S. T., Hunter J. H., 1990, ApJ, 348, 456
- Eskridge P. B. et al., 2000, AJ, 119, 536
- Fasano G., Amico P., Bertola F., Vio R., Zeilinger W. W., 1993, MNRAS, 262, 109
- Franx M., de Zeeuw T., 1992, ApJ, 392, L47
- Franx M., van Gorkom J. H., de Zeeuw T., 1994, ApJ, 436, 642
- Gerssen J., 2002, in E. Athanassoula, A. Bosma & R. Mújica, eds, ASP Conf. Ser. Vol. 275, Disks of Galaxies: Kinematics, Dynamics and Perturbations. Astron. Soc. Pac., San Francisco, pg. 197
- Gerssen J., Kuijken K., Merrifield M. R., 1999, MNRAS, 306, 926
- Grosbøl P. J., 1985, A&AS, 60, 261
- Huizinga J. E., van Albada T. S., 1992, MNRAS, 254, 677
- Kent S. M., 1987, AJ, 93, 1062
- Knapen J. H., 1999, in J. E. Beckman, & T. J. Mahoney, eds, ASP Conf. Ser. Vol. 187, The Evolution of Galaxies on Cosmological Timescales. Astron. Soc. Pac., San Francisco, p. 72
- Kuijken K., Tremaine S., 1994, ApJ, 421, 178
- Lambas D. G., Maddox S. J., Loveday J., 1992, MNRAS, 258, 404
- Lindblad P. A. B., Kristen H., 1996, A&A, 313, 733
- Lindblad P. A. B., Lindblad P. O., Athanassoula E., 1996, A&A, 313, 65
- Magrelli G., Bettoni D., Galletta G., 1992, MNRAS, 256, 500
- Mathewson D. S., Ford V. L., 1996, ApJS, 109, 97
- Merrifield M. R., Kuijken K., 1995, MNRAS, 274, 933
- Palunas P., Williams, T. B., 2000, AJ, 120, 2884
- Prendergast K. H., Tomer E., 1970, AJ, 75, 674
- Rix H.-W., Zaritsky D., 1995, ApJ, 447, 82
- Sakai S. et al., 2000, ApJ, 529, 698
- Schoenmakers R. H. M., Franx M., de Zeeuw T., 1997, MNRAS, 292, 349
- Schwarz U. J., 1985, A&A, 142, 273
- Sellwood J. A., Valluri M., 1997, MNRAS, 287, 124
- Tremaine S., Weinberg M. D., 1984, ApJ, 282, L5
- Tully R. B., Fisher J. R., 1977, A&A, 54, 661
- Valenzuela O., Klypin A., 2002, MNRAS, *submitted* (astro-

ph/0204028)

van Albada T. S., Sanders R. H., 1982, MNRAS, 201, 303

Weinberg M. D., 1985, MNRAS, 213, 451

Weiner B. J., Sellwood J. A., Williams T. B., 2001, ApJ, 546, 931